PERGAMON

International Journal of Heat and Mass Transfer 42 (1999) 2327–2336

International Journal of
HEAT and MASS
TRANSFER

Pseudosteady-state natural convection inside spherical containers partially filled with a porous medium

Y. Zhang[1], J.M. Khodadadi*, F. Shen[2]

Department of Mechanical Engineering, Auburn University, 201 Ross Hall, Auburn, AL 36849-5341, U.S.A.

Received 3 October 1997; in final form 22 September 1998

Abstract

A computational study of the pseudosteady-state two-dimensional natural convection within spherical containers partially filled with a porous medium is presented. The computations are based on an iterative, finite-volume numerical procedure using primitive dependent variables, whereby the time-dependent continuity, momentum and energy equations in the spherical coordinate system are solved within the composite system. The natural convection effect is modeled via the Boussinesq approximation, whereas the Darcy Law is utilized to treat the porous medium. For a reference case, flow and temperature field details during the transient evolution to the pseudosteady-state are presented. It is shown that the dominant transport mechanism at the early stages is due to heat conduction and natural convection plays no role. A parametric study was performed with the values of the Rayleigh number (*Ra*), Darcy number (*Da*) and the thermal conductivity ratio varying one at a time. The dependence of the flow and thermal fields on these parameters was elucidated. For low *Ra* and *Da* numbers, the flow field is restricted within the central fluid core. Only for high *Ra* and *Da* numbers, one can observe comparable fluid motion in both the porous medium and central fluid core regions. The local Nusselt number on the surface and interface temperature exhibit nearly uniform variations for low *Ra* and *Da* numbers, signifying little deviation from the limiting pure conduction case. For high *Ra* and *Da* numbers, marked heat transfer is observed on the bottom of the sphere. The interface temperature is also seen to deviate from uniform variation for high *Ra* and *Da* numbers. Only the intensity of the recirculating flow in the central fluid core region was seen to depend on the thermal conductivity ratio. The thermal conductivity ratio modifies the time scale of the thermal transport and only the relative magnitudes of the monitored quantities are affected. © 1999 Elsevier Science Ltd. All rights reserved.

Nomenclature

c_p	specific heat at constant pressure [J kg^{-1} K^{-1}]
g	gravitational acceleration [m s^{-2}]
k	thermal conductivity [W m^{-1} K^{-1}]
K	permeability [m^2]
Nu_m	mean Nusselt number, equation (16)
p	pressure [Pa]
p_0	static pressure [Pa]
r	radial coordinate within the sphere [m]
R	radius of the sphere [m]
t	time [s]
t^*_{pss}	dimensionless time needed to reach the pseudo-steady-state condition
T	temperature [K]
T_m	mean or bulk temperature of the fluid [K]
T_0	initial temperature of the fluid [K]
V_r	radial component of the fluid velocity [m s^{-1}]
V_θ	polar component of the fluid velocity [m s^{-1}].

Greek symbols

β	coefficient of thermal expansion [K^{-1}]
θ	polar angle in the sphere
ν	kinematic viscosity [m^2 s^{-1}]
ρ	density [kg m^{-3}].

Subscripts

e	effective quantity for the fluid-saturated porous medium
r	radial component

---

* Corresponding author. Tel.: 001 334 844 3333; fax: 001 334 844 3307; e-mail: jkhodada@eng.auburn.edu

[1] Currently ICEM CFD, Westland, MI, U.S.A.

[2] Currently with Adapco, Inc., Melville, NY, U.S.A.

PII: S0017-9310(98)00328-7

s related to the solid matrix
θ polar component.

1. Introduction

Spherical shapes and containers are widely used and/or encountered in industrial applications and naturally-occurring phenomena. Accordingly, greater understanding of the fluid flow and heat transfer within spheres should prove extremely useful in a variety of disciplines. These include spray forming, fuel droplet vaporization, fluid storage and mixing tank modeling, containerless processing and environmental transport applications. There are also numerous applications such as geothermal systems, thermal insulations and specific materials processing techniques such as spray forming and powder metallurgy where partially or fully-saturated composite fluid-porous media formations are encountered.

Going through the literature, it is apparent that very little attention has been given to natural convection inside spherical containers. Pustovoit [1] proposed an approximate method to solve the equations governing slowly-varying axisymmetric natural convection inside a spherical container by expanding the dependent variables in terms of the Grashof number series. The resulting linear equations were solved by successive approximations. With the initial liquid temperature being higher than the constant surface temperature, the liquid which was being cooled sank near the surface, whereas the hotter liquid rose vertically in the middle of the sphere. It was observed that the liquid was cooled least in a region located at about one third of the radius above the center, where molecular conduction was dominant. Whitley and Vachon [2] published their numerical solutions of transient axisymmetric laminar natural convection heat transfer inside spheres using the Boussinesq approximation. A finite-difference-based vorticity-stream function numerical procedure was employed. The fluid which was initially at a constant temperature was suddenly subjected to a steep rise in the wall temperature. In this configuration, the fluid being heated next the surface rose upward, replacing the colder fluid which sank vertically to the bottom of the sphere. Chow and Akins [3] presented experimental results of the pseudosteady-state natural convection inside spheres. The distinct feature of the pseudosteady-state treatment is that the driving force for convection is kept constant, i.e. the temperature outside the sphere was increased steadily so that the temperature difference between the outside and the center of the sphere remained constant. During the flow visualization phase of the study, the motion of hollow glass spheres were monitored and the location of the eye of the recirculation pattern was quantified. They also provided an empirical correlation for the mean Nusselt number in the laminar regime (Rayleigh number below 10^7). Hutchins and Marschall [4] presented computational results for pseudosteady-state, two-dimensional, natural convection inside spheres. Using a finite-difference-based vorticity-stream function numerical procedure similar to Whitley and Vachon [2], they simulated the flow and temperature fields in the laminar regime (Rayleigh number between 10^5–10^8) and two different Prandtl numbers of 0.7 and 8. The general trends of their computed eye of the recirculation and mean Nusselt number variation were similar to the findings of Chow and Akins [3]. The heat transfer data were found to be independent of the Prandtl number and a mean Nusselt number correlation applicable for the Rayleigh number range of 10^5–10^8 was proposed. Shen et al. [5] performed a set of pseudosteady-state computations of natural convection within spherical containers, very similar to the computational study of Hutchins and Marschall [4], with the main distinction being the use of a finite-volume primitive-variables-based methodology. In addition to comparing the results to the previously-published data of Hutchins and Marschall [4], and experimental findings of Chow and Akins [3], the surface heat transfer characteristics along with the details of the transient evolution to the pseudosteady-state conditions were elucidated. Nguyen et al. [6] recently analyzed transient natural convection in a spherical container composite system which was partially filled with a porous medium. Using a hybrid spectral method, they numerically simulated the unsteady fluid flow and heat transfer behavior within spherical containers. They concluded that the heat transfer results were not sensitive to the variation of the Prandtl number for the range considered (0.5–10). It was established that the overall heat transfer rate was primarily controlled by the transport characteristics in the porous medium and the thermal conductivity ratio.

Partly motivated by the recent paper of Nguyen et al. [6] and in order to extend the previous work of the authors [5], the present study was undertaken to elucidate the pseudosteady-state form of natural convection within spherical containers partially filled with a porous medium. Such an investigation has not been reported to date. The results can have immediate application in specific problems such as transport of geological formations associated with nuclear waste repositories [6], modeling of geothermal systems and phase change within droplets.

2. Mathematical formulation

Consider a spherical container with radius of R, which is partially filled with a porous medium extending from $r = r_f$ to $r = R$. The container is completely filled with a fluid, thus the inner core ($r < r_f$) is void of the porous material. Given the following assumptions: (1) Being symmetric with respect to the azimuthal direction ϕ, the dependent variables are functions of the radial position (r) and the polar angle (θ). (2) The fluid is viscous and Newtonian. The fluid properties are constant except for the variation of density which is modeled using the Boussinesq approximation and viscous heating effects are ignored. (3) The porous medium is homogeneous and isotropic. The fluid and the solid matrix within the porous medium are in local thermal equilibrium.

The appropriate volume-averaged transport equations within the porous medium in the spherical coordinate system can be developed. The details are not provided here, but can be found elsewhere, i.e. Vafai and Tien [7]. Two sets of governing equations are needed to describe the present composite system which consists of a pure fluid inner core and the porous medium outer shell. In order to avoid repetition, a general equation for both regions is written followed by a description of the main distinctions. The continuity equation is:

$$\frac{1}{r^2}\frac{\partial}{\partial r}(r^2 V_r)+\frac{1}{r\sin\theta}\frac{\partial}{\partial\theta}(V_\theta\sin\theta)=0 \tag{1}$$

The momentum equation in the polar direction (θ) is:

$$\begin{aligned}\rho\left(\frac{\partial V_\theta}{\partial t}+V_r\frac{\partial V_\theta}{\partial r}+\frac{V_\theta}{r}\frac{\partial V_\theta}{\partial\theta}+\frac{V_rV_\theta}{r}\right)&=-\frac{1}{r}\frac{\partial(p-p_0)}{\partial\theta}\\&+\rho\nu\left[\nabla^2V_\theta+\frac{2}{r^2}\frac{\partial V_r}{\partial\theta}-\frac{V_\theta}{r^2\sin^2\theta}\right]\\&-\rho\beta g_\theta(T-T_0)+S_{\mathrm{D}\theta}\end{aligned}\tag{2}$$

where

$$\nabla^2=\frac{1}{r^2}\frac{\partial}{\partial r}\left(r^2\frac{\partial}{\partial r}\right)+\frac{1}{r^2\sin\theta}\frac{\partial}{\partial\theta}\left(\sin\theta\frac{\partial}{\partial\theta}\right).\tag{3}$$

The momentum equation in the radial direction (r) is:

$$\begin{aligned}\rho\left(\frac{\partial V_r}{\partial t}+V_r\frac{\partial V_r}{\partial r}+\frac{V_\theta}{r}\frac{\partial V_r}{\partial\theta}-\frac{V_\theta^2}{r}\right)&=-\frac{\partial(p-p_0)}{\partial r}\\&+\rho\nu\left[\nabla^2V_r-\frac{2}{r^2}V_r-\frac{2}{r^2}\frac{\partial V_\theta}{\partial\theta}-\frac{2\cot\theta}{r^2}V_\theta\right]\\&-\rho\beta g_r(T-T_0)+S_{\mathrm{D}r}\end{aligned}\tag{4}$$

Finally, the energy equation is:

$$\begin{aligned}(\rho c_{\mathrm{p}})'\frac{\partial T}{\partial t}+\rho c_{\mathrm{p}}\left(V_r\frac{\partial T}{\partial r}+\frac{V_\theta}{r}\frac{\partial T}{\partial\theta}\right)\\=k'\left[\frac{1}{r^2}\frac{\partial}{\partial r}\left(r^2\frac{\partial T}{\partial r}\right)+\frac{1}{r^2\sin\theta}\frac{\partial}{\partial\theta}\left(\sin\theta\frac{\partial T}{\partial\theta}\right)\right]\end{aligned}\tag{5}$$

Table 1
Representation of the variables within different regions

	Fluid region	Porous medium
V_r, V_θ and T	Fluid variables	Volume-averaged quantities
$S_{\mathrm{D}r}$	0	$-\frac{\mu}{K}V_r$
$S_{\mathrm{D}\theta}$	0	$-\frac{\mu}{K}V_\theta$
$(\rho c_{\mathrm{p}})'$ k'	ρc_{p} k	$\rho_{\mathrm{e}}c_{\mathrm{e}}$ k_{e}

In the foregoing equations, distinction must be made between the fluid velocity within the pure fluid and within the porous medium. Table 1 is provided in order to distinguish the meaning of the various variables within the two zones. It should be noted that the Darcy Law is used to treat the porous material, through the introduction of friction terms ($S_{\mathrm{D}r}$ and $S_{\mathrm{D}\theta}$) in the two momentum equations. The quantity K is the permeability of the porous medium and is given by

$$K=\frac{\mu\lambda^3}{C(1-\lambda)^2}\tag{6}$$

where λ is the porosity of the medium. Within the fluid, the porosity has the value of 1, whereas within the porous medium the porosity is less than 1. The quantity C is the porosity constant and its value varied between 3×10^5 and 5.2×10^7 during the computations.

Introducing the following dimensionless variables with use of the superscript (*):

$$r^*=\frac{r}{R}\quad V^*=\frac{RV}{\alpha}\quad t^*=\frac{\alpha t}{R^2}\quad p^*=\frac{R^2p}{\rho\alpha^2}\quad \Theta=\frac{T-T_0}{T_{\mathrm{w}}-T_{\mathrm{c}}}\tag{7}$$

where α is the thermal diffusivity, the dimensionless governing equations in vector form are obtained:

$$\nabla\bullet\mathbf{V}^*=0\tag{8}$$

$$\frac{\partial\mathbf{V}^*}{\partial t^*}+\mathbf{V}^*\bullet\nabla^*\mathbf{V}^*=-\nabla^*p^*+Pr\nabla^{*2}\mathbf{V}^*+\frac{1}{8}RaPr\Theta\mathbf{e}_{\mathrm{g}}-\frac{Pr}{Da}\mathbf{V}^*\tag{9}$$

where $\mathbf{e}_{\mathrm{g}}$ is the unit vector in the direction of the gravitational acceleration and:

$$Pr=\frac{\nu}{\alpha}\quad Ra=\frac{8g\beta(T_{\mathrm{w}}-T_{\mathrm{c}})R^3}{\nu\alpha}\quad Da=\frac{K}{R^2}\tag{10}$$

are the Prandtl, Rayleigh and Darcy numbers, respectively. The dimensionless energy equation is:

$$\Phi_{\mathrm{c}}\frac{\partial\Theta}{\partial t^*}+\mathbf{V}^*\bullet\nabla^*\Theta=\Phi_k\nabla^{*2}\Theta\tag{11}$$

where Φ_{c} and Φ_k are defined as:

$$\Phi_{\mathrm{c}}=\lambda+(1-\lambda)\frac{(\rho c_{\mathrm{p}})_{\mathrm{s}}}{\rho c_{\mathrm{p}}}\quad \Phi_k=\frac{k_{\mathrm{e}}}{k_{\mathrm{s}}}.\tag{12}$$

Within the fluid region, the Darcy number is equal to infinity, $\Phi_c = \Phi_k = 1$, and the governing equations above represent the well established formulation for classic natural convection.

2.1. Boundary and initial conditions

The fluid flow boundary condition on the solid surface is the no-slip condition, that is:

$$V_r^* = V_\theta^* = 0 \quad \text{at} \quad r^* = 1 \quad \text{for} \quad t^* > 0 \tag{13}$$

To ensure the maintenance of the pseudosteady-state condition, the temperature on the surface (T_w) was allowed to vary with time so that it was always above the temperature of the center of the sphere (T_c) by a constant value. The boundary conditions at the physical symmetry axis of the sphere are:

$$V_r^* = \frac{\partial V_\theta^*}{\partial \theta} = \frac{\partial \Theta}{\partial \theta} = 0 \quad \text{at} \quad \theta = 0, \pi \tag{14}$$

The problem associated with the variables being multi-valued at the center is removed by introducing a very small, but finite, interior surface. The validity of this technique was discussed by de Vahl Davis [8]. The axial symmetric boundary condition is applied at the interior surface. On all the boundaries of the computational domain, the gradient boundary conditions were discretized by using a three-point formula with second order of accuracy. At the beginning of the computations ($t^* = 0$), the fluid velocity was set to zero and the fluid temperature was fixed at a constant value (T_0), thus:

$$V_r^* = V_\theta^* = 0 \quad \Theta = 0 \quad \text{for} \quad 0 < r^* < 1 \quad \text{at} \quad t^* = 0 \tag{15}$$

2.2. Computational details

The numerical solution of the governing transport equations was obtained following the SIMPLE procedure of Patankar [9]. A 31 × 41 grid system was chosen following a systematic parametric study with other grid densities (21 × 31 and 41 × 51). The final choice of the grid density was based on comparison among the predictions of the transient velocity and temperature at three polar angle locations. In addition, a similar grid density was already proven to be very adequate in matching the previous experimental [3] and computational [4] studies. Thirty-one uniform grids were laid in the θ direction from 0 to π in 6° increments. A hybrid of uniform and non-uniform grids were laid in the radial direction for the intervals $r^* = 0$–0.3, 0.3–0.5, 0.5–0.75 and 0.75–1, in order to capture the pertinent details in the fluid core, fluid-porous medium interface and near the solid surface. The schematic diagram of the computational grid system is shown in Fig. 1. The gravitational acceleration vector points vertically downward along the $\theta = \pi$ line. The temporal derivatives were treated using an implicit formulation. The time step used in the computations was maintained at 0.1 s. The line-by-line method was used to obtain converged solutions iteratively, whereas relaxation factors of 0.1, 0.1, 0.15 and 0.15 were used for V_r, V_θ, P and T, respectively. At every time step, the iterations were terminated when the sum of the normalized absolute residuals for each variable was less than 10^{-6}. In addition, the relative change of all the variables at every grid point were assured to be lower than 10^{-5} upon convergence. At each time step, the number of iterations needed to achieve convergence varied between 200 and 2000. The CPU time per iteration was 1.5×10^{-1} s, which is about an order of magnitude greater than those for pure fluid computations [5]. The computations were performed on the CRAY C-90 supercomputer of the Alabama Super-

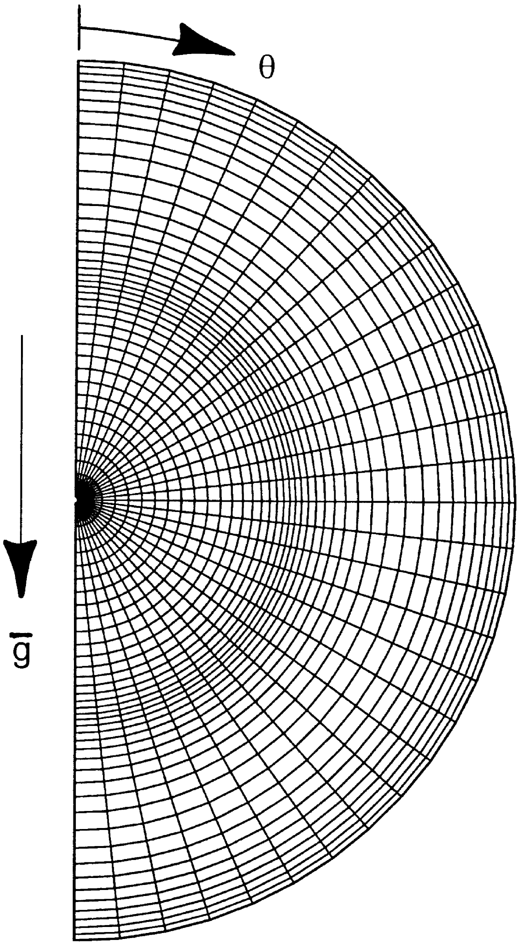

Fig. 1. Schematic diagram of the computational grid system.

computer Authority, which is located in Huntsville, Alabama.

3. Results and discussion

In the beginning, a brief overview of the behavior of pseudosteady-state natural convection for pure fluids within spherical containers is given. These results are similar to those of [5] and are given in order to establish a reference state for the limiting case of composite systems.

3.1. Pure fluid systems without porous medium

Even though the pseudosteady-state results presented in this paper for composite systems and earlier for pure fluid systems [5] are obtained by performing transient calculations, the time-dependent evolution of the velocity and temperature fields leading to the pseudosteady-state condition should not be ignored. Early in the process, the fluid responds to the step change in the wall temperature by forming concentric temperature contours, independent of the polar angle. This suggests that during the early periods, the dominant transport phenomena is due to heat conduction and natural convection plays a small role. As time progresses, natural convection proves dominant and the concentric temperature contours become skewed, the degree of which depends on the magnitude of the Rayleigh number. After a time period, the system will attain the pseudosteady-state condition. In our computations, similar to those of Hutchins and Marschall [4], the attainment of the pseudosteady-state condition was decided by monitoring the value of the mean Nusselt number (Nu_m), defined as:

$$Nu_m = \frac{1}{2}\int_0^\pi \left[\frac{\partial T^*}{\partial r^*}\right]_{r^*=1} \sin\theta \, d\theta \quad \text{with} \quad T^* = \frac{T - T_0}{T_w - T_m} \tag{16}$$

The pseudosteady-state condition was established once the relative change in the value of the mean Nusselt number over a time step was less than 10^{-6}. The dimensionless time needed to achieve the pseudosteady-state condition (t^*_{pss}) ranged between 0.33 ($Ra = 10^5$) and 0.04 ($Ra = 10^7$). The composite diagrams of the streamline and temperature field contours under pseudosteady-state condition for the case of $Pr = 4.16$ and the Rayleigh numbers of 10^5, 10^6 and 10^7 are presented in Fig. 2a–c. The streamlines are shown on the left half of the sphere, whereas the respective temperature field contours are drawn on the right half of the sphere. For the Rayleigh number of 10^5 (Fig. 2a), one can see that the temperature contours are skewed from a concentric ring distribution suggesting that natural convection effects are important. As buoyancy-induced convection becomes more dominant, the temperature contour deviations from concentric ring patterns become more marked and the temperature gradients become more pronounced on the bottom of the sphere. One can clearly observe that the fluid being heated adjacent to the surface rises, replacing the colder fluid which sinks downward along the center of the sphere. For the high Rayleigh number flows (Fig. 2b and c), the crescent-shaped pattern of recirculating flow was found to be in good agreement with the experimental results of Chow and Akins [3]. The location of the eye of the recirculation pattern is observed to be dependent on the Rayleigh number and moves toward the surface as natural convection is intensified. This is accompanied by appearance of strong shearing of the velocity field between the surface and the eye of the recirculation pattern.

3.2. Composite fluid–porous medium systems

For the present set of computations the porous medium extends from $r^* = r_f/R = 0.5$ to 1 similar to the study of Nguyen et al. [6]. In light of the previous findings [4–6], who have demonstrated the weak dependence of the results on the Prandtl number, parametric studies were performed only for a Prandtl number of 4.16 (water at 315 K). Given the fluid with known properties, a parametric study of the remaining dimensionless parameters (Da, Ra and Φ_k) was performed. A reference case with typical assigned dimensionless parameters was selected which is summarized in the second column of Table 2. The range of variations of Da, Ra and Φ_k are outlined in the third column of Table 2. The chosen range of variation of the Rayleigh number (10^5–10^8) is in line with earlier studies [3, 5]. Choice of the variation ranges for Da and Φ_k is consistent with the study of Nguyen et al. [6]. The dimensionless times needed to reach the pseudosteady-state condition (t^*_{pss}) varied between 0.016 and 0.187 (summarized in the fourth column of Table 2).

3.2.1. Transient fluid flow results for the reference case

The time-dependent evolution of the velocity vectors and streamlines leading to the pseudosteady-state condition for the reference case is illustrated in Fig. 3a–d at different time instants. In these figures, the solid inner circle is the position of the porous medium interface located at $r^* = 0.5$. The dimensionless time instances discussed in Fig. 3a–d correspond to (a) 0.0048 (b) 0.024 (c) 0.034 and (d) 0.077. Early in the process ($t^* = 0.0048$), the fluid responds to the sudden step change in the surface temperature by rising along the surface. The fluid velocity near the surface is high due to the steep temperature gradient there. The heated fluid which rose to the top will then fall along the symmetry axis from the porous medium into the central fluid core. At this early time instant ($t^* = 0.0048$), the fluid velocity magnitudes within the central fluid core appear to be comparable to those observed near the surface, partly

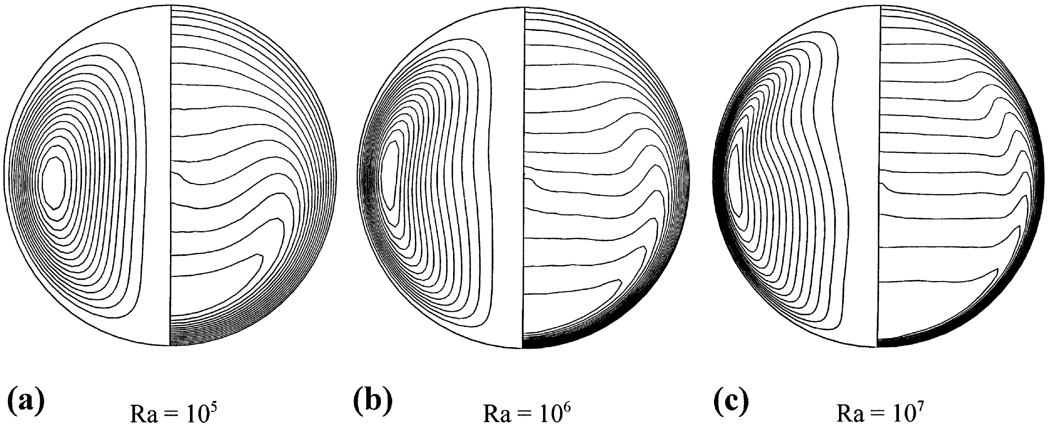

Fig. 2a–c. Pseudosteady-state streamline and temperature field contours for pure fluid systems for the Rayleigh numbers of (a) 10^5, (b) 10^6 and (c) 10^7.

Table 2
Variation of the dimensionless parameters

	Reference case ($t^*_{\text{pss}} = 0.072$)	Range of variation	$t^*_{\text{pss}} \times 10^2$
Da	10^{-5}	10^{-3}, 10^{-4}, 10^{-6}, 10^{-7}	18.7, 17.6, 5.8, 5.1
Ra	10^6	10^5, 10^7, 10^8	7.1, 4.6, 1.6
Φ_k	0.7	1, 2, 5	8.1, 9.2, 9.6
λ	0.75	unchanged	
Φ_c	1	unchanged	

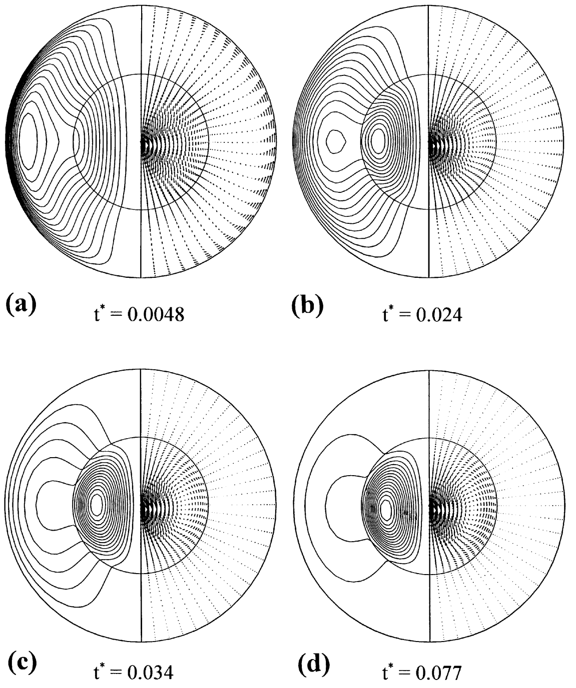

Fig. 3a–d. Transient evolution of the velocity vectors and streamline contours for the reference case ($Ra = 10^6$, $Da = 10^{-5}$ and $\Phi_k = 0.7$) at dimensionless time instants (a) 0.0048 (b) 0.024 (c) 0.034 and (d) 0.077.

due to natural convection and partly due to the fact that in spherical geometry the available cross-sectional areas decrease as one moves toward the center. The fluid within the porous medium which is set in motion due to the buoyancy effect will encounter resistance to its motion proportional to its speed. With the rise in this resistance, the fluid will prefer to avoid travel through the porous medium and establishes itself within the central fluid core ($r^* < 0.5$). Note that after the pseudosteady-state condition is reached for the reference case ($t^* = 0.077 > t^*_{\text{pss}} = 0.072$), the bulk of the fluid has migrated inward and the large recirculatory eddy of the early period has shrunk in size to occupy the space within the central fluid core.

3.2.2. Pseudosteady-state fluid flow and heat transfer results

The composite diagrams of the streamlines and temperature field contours for the Rayleigh numbers of 10^5, 10^6, 10^7 and 10^8 are presented in Fig. 4a–d, where the Darcy number and the thermal conductivity ratio are kept at the values of the reference case. For the lowest value of the Rayleigh number ($Ra = 10^5$, Fig. 4a) studied, nearly perfect concentric temperature contours are observed, indicating one-dimensional heat diffusion. For the Rayleigh number of 10^6 (the reference case), one can see that the temperature contours are skewed to some extent from a concentric ring distribution. For both Ray-

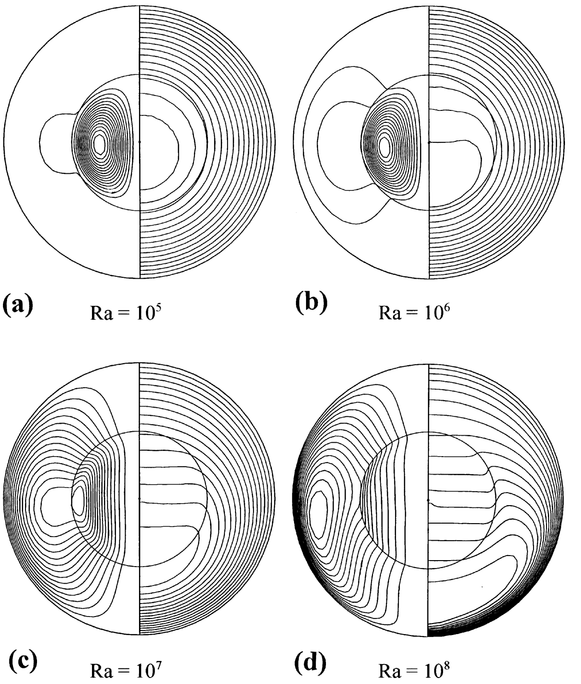

(a) Ra = 10^5 (b) Ra = 10^6

(c) Ra = 10^7 (d) Ra = 10^8

Fig. 4a–d. Pseudosteady-state streamline and temperature field contours for composite systems, corresponding to the Rayleigh numbers of (a) 10^5 (b) 10^6 (c) 10^7 and (d) 10^8 ($Da = 10^{-5}$ and $\Phi_k = 0.7$).

leigh numbers of 10^5 and 10^6, the streamlines are concentrated within the central fluid core. This signifies that the fluid having encountered—on its course of attaining the pseudosteady-state condition—the resistance offered within the porous medium has established itself within the central fluid core. As buoyancy-induced convection becomes more dominant, the temperature contour deviations from concentric ring patterns become more marked and the temperature gradients become more pronounced on the bottom of the sphere similar to the findings for pure fluid systems [5]. For the high Rayleigh number cases presented in Fig. 4c, d, the temperature field within the central fluid core is made up of isothermal horizontal layers. This is brought about by the dominance of the buoyancy force which can negotiate its way through the porous medium and therefore, penetrates further into the porous medium region as the Rayleigh number increases. The location of the eye of the recirculation pattern is observed to be dependent on the Rayleigh number and moves toward the surface and into the porous medium as natural convection is intensified. This phenomenon is further clarified in Fig. 5a, where the variations of the dimensionless polar velocity component (V_θ^*) along the horizontal plane going through the center of the sphere are given for the Rayleigh numbers of 10^5, 10^6 and 10^7. For the Rayleigh numbers of 10^5 and 10^6, the fluid within the porous medium ($r^* > 0.5$) is slow-moving due to the resistance in this zone and the weakness of the natural convection force to negotiate it. On

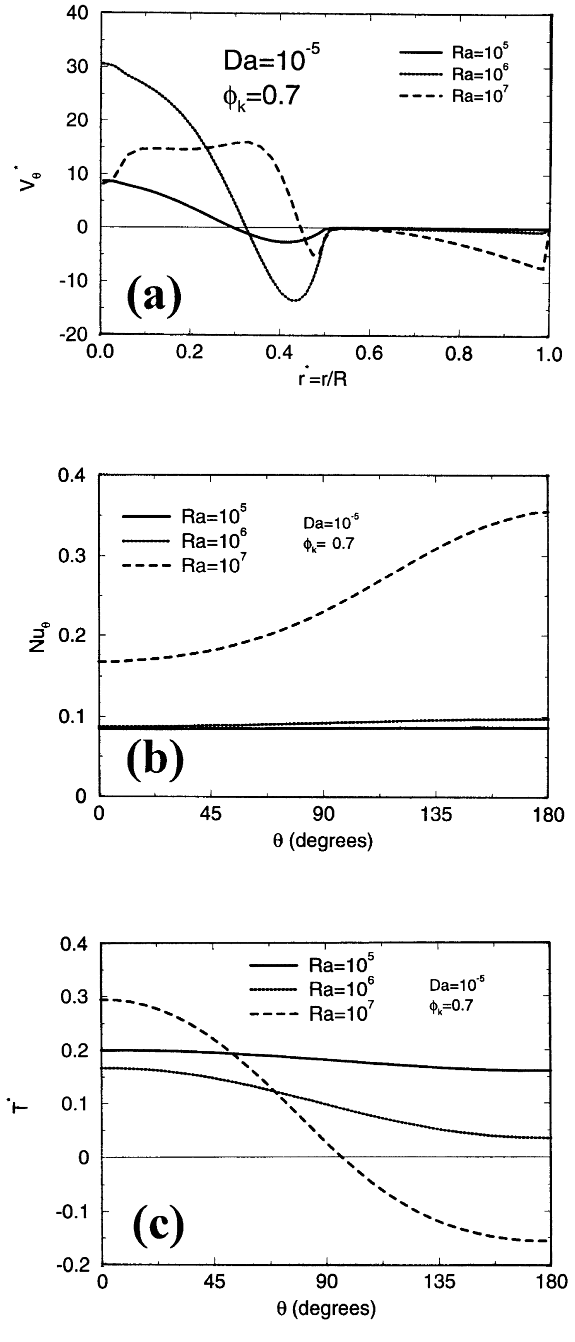

Fig. 5a–c. Pseudosteady-state variations of (a) velocity component (V_θ^*) along the horizontal plane ($\theta = \pi/2$) (b) the local surface Nusselt number and (c) the interface temperature, for the Rayleigh numbers of 10^5, 10^6 and 10^7 ($Da = 10^{-5}$ and $\Phi_k = 0.7$).

the other hand, the fluid velocity within the central fluid core ($r^* < 0.5$) is marked in comparison, in addition to exhibiting the recirculating nature of the flow field in this zone. For the high Rayleigh number of 10^7, the strengthened buoyancy force resulting from the steep temperature gradients within the porous medium is capable of negotiating the resistance force and the fluid motion is intensified within the porous medium. At the same time, the fluid velocity within the central fluid core has diminished.

The variations of the local Nusselt number

$$\left(Nu_\theta = \frac{\partial T^*}{\partial r^*}\bigg|_{r^*=1}\right) \tag{17}$$

on the surface of the sphere for the Rayleigh numbers of 10^5, 10^6 and 10^7 are given in Fig. 5b. For the Rayleigh numbers of 10^5 and 10^6, the heat transfer rates appear to be very weakly dependent on the position on the surface. On the other hand, for the high Rayleigh number of 10^7, gravity-induced fluid motion greatly enhances the heat transfer rate near the bottom of the sphere, where steep temperature gradients are observed. The influence of the natural convection in modifying the temperature field is illustrated in Fig. 5c, where the pseudosteady-state interface temperature at $r^* = 0.5$ is presented as a function of the polar angle for the Rayleigh numbers of 10^5, 10^6 and 10^7. The case of the low Rayleigh number (10^5) shows very little deviation from the limiting case of pure heat conduction. As natural convection becomes dominant, the interface temperature becomes more skewed.

The variations of the dimensionless polar velocity component along the horizontal plane going through the center of the sphere are given for the Darcy numbers of 10^{-4}, 10^{-5}, 10^{-6} and 10^{-7} in Fig. 6a. For the low Darcy numbers studied, the flow field is mainly concentrated within the central fluid core. Only for the case of high Darcy number of 10^{-4}, one can observe comparable fluid motion in both the porous medium and central fluid core regions. The variations of the local Nusselt number on the surface of the sphere for the Darcy numbers of 10^{-4}, 10^{-5}, 10^{-6} and 10^{-7} are presented in Fig. 6b. As expected, the cases corresponding to the low Darcy numbers exhibit nearly uniform heat transfer rates on the surface of the sphere. For the high Darcy number of 10^{-4}, noticeable heat transfer is observed on the bottom of the sphere due to the steep temperature gradients there. The pseudosteady-state interface temperature is presented as a function of the polar angle for the Darcy numbers of 10^{-4}, 10^{-5}, 10^{-6} and 10^{-7} in Fig. 6c. The extent of deviation from uniform variation is very marked for the high Darcy number case which accommodates the marked deviation from the concentric temperature contour pattern.

The variations of the dimensionless polar velocity component along the horizontal plane going through the center of the sphere are given for the thermal conductivity ratios of 0.7, 1, 2 and 5 in Fig. 7a. For all these cases with

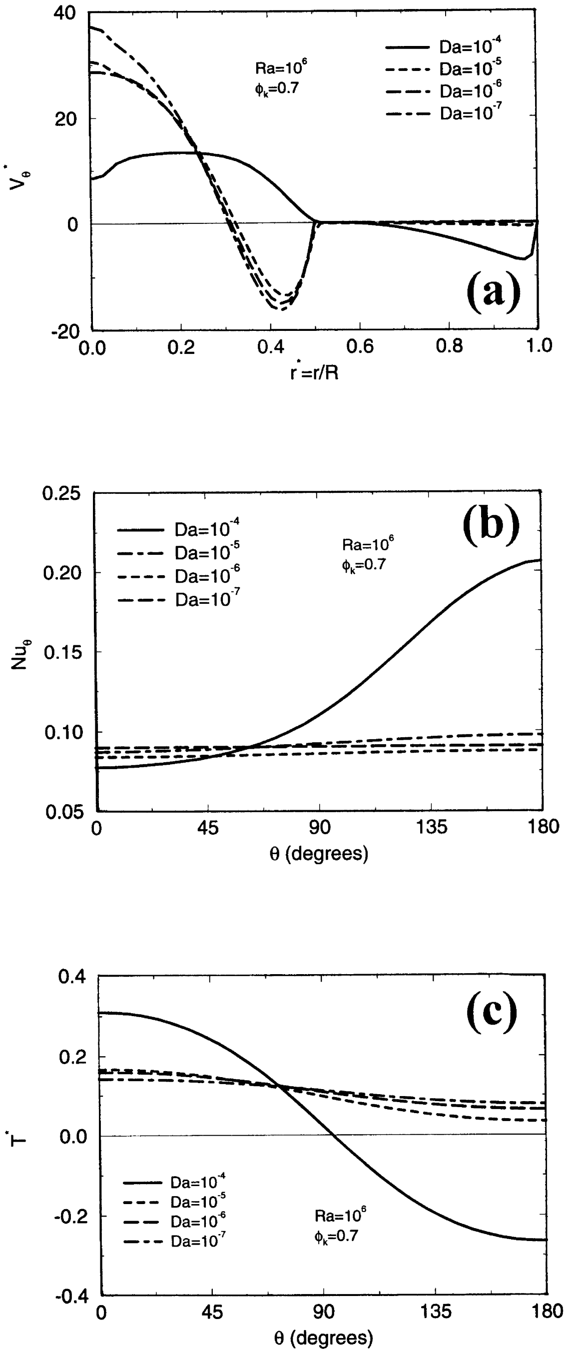

Fig. 6a–c. Pseudosteady-state variations of (a) velocity component (V^*_θ) along the horizontal plane ($\theta = \pi/2$) (b) the local surface Nusselt number and (c) the interface temperature, for the Darcy numbers of 10^{-4}, 10^{-5}, 10^{-6} and 10^{-7} ($Ra = 10^6$ and $\Phi_k = 0.7$).

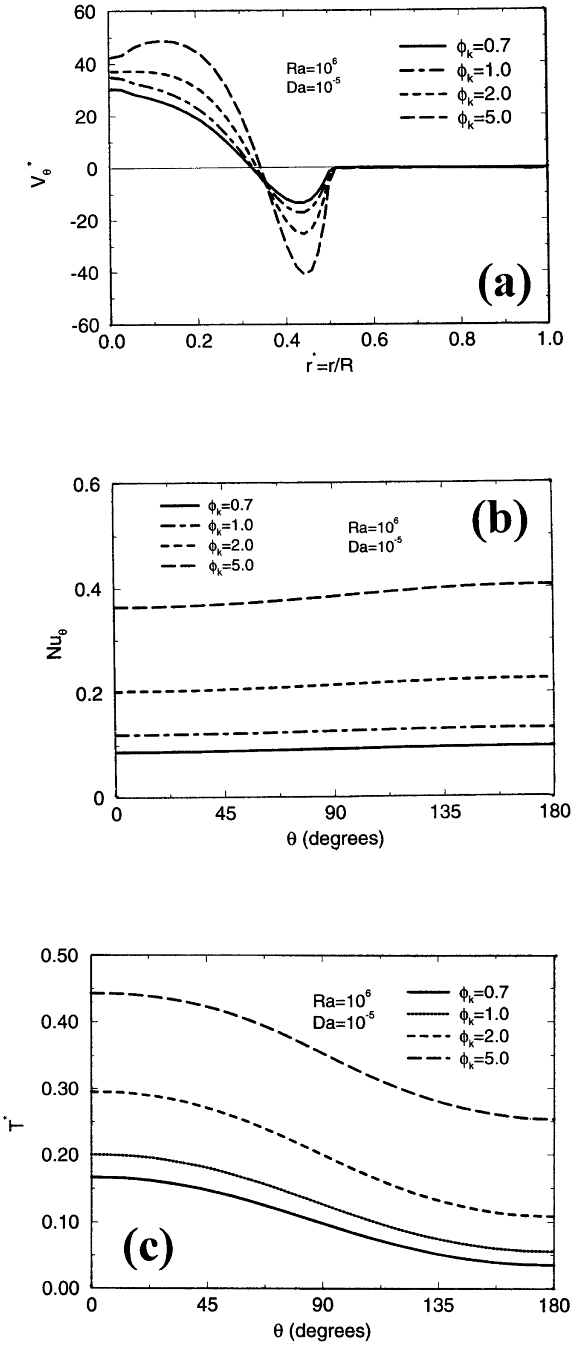

Fig. 7a–c. Pseudosteady-state variations of (a) velocity component (V_θ^*) along the horizontal plane ($\theta = \pi/2$) (b) the local surface Nusselt number and (c) the interface temperature, for the thermal conductivity ratios of 0.7, 1, 2 and 5 ($Ra = 10^6$ and $Da = 10^{-5}$).

$Ra = 10^6$ and $Da = 10^{-5}$, the fluid motion is restricted to the central fluid core and only the intensity of the recirculating flow is seen to depend on the thermal conductivity ratio. This dependence is brought about by the buoyancy term in the momentum equations, which in turn is coupled to the energy equation which includes the thermal conductivity ratio. The variations of the local Nusselt number on the surface of the sphere for the thermal conductivity ratios of 0.7, 1, 2 and 5 are given in Fig. 7b. The local Nusselt number variations for different thermal conductivity ratios are similar to each other and only the relative magnitudes are different. This should not be surprising since the thermal conductivity ratio only appears on the advection side of the energy equation and being a constant just modifies the time scale of the thermal transport. A similar behavior is observed for the pseudosteady-state interface temperature which is presented in Fig. 7c as a function of the polar angle for the thermal conductivity ratios of 0.7, 1, 2 and 5. For a given polar angle, as the thermal conductivity ratio is increased, the dimensionless interface temperature rises. In essence, as the thermal conductivity of the porous medium increases, resistance to thermal transport is lowered and higher interface temperatures are observed.

4. Conclusions

The following conclusions are drawn for the pseudosteady-state natural convection within spherical containers partially filled with a porous medium:

(1) During the transient period before attaining the pseudosteady-state condition, the heated fluid within the porous medium adjacent to the surface rises replacing the colder fluid which sinks from the porous medium into the central fluid core. With the rise in the resistance offered to the fluid in the porous medium, the fluid establishes itself within the central fluid core.

(2) Under the pseudosteady-state condition, nearly perfect concentric temperature contours are observed for low *Ra*, indicating one-dimensional heat diffusion. As buoyancy-induced convection becomes dominant, the temperature contours' deviations from concentric ring patterns become more marked and the temperature gradients become more pronounced on the bottom of the sphere. For low *Ra*, the fluid motion within the porous medium is slow due to the resistance in this zone. For high *Ra*, the strengthened buoyancy force is capable of negotiating the resistance force and the fluid motion is intensified within the porous medium. The surface heat transfer rate and interface temperature appear to be weakly dependent on the position for low *Ra*, signifying little deviation from the limiting pure conduction case. For high *Ra*, gravity-induced fluid motion greatly

enhances the heat transfer rate near the bottom of the sphere. In addition, the interface temperature becomes more skewed.

(3) For low *Da*, the flow field is restricted within the central fluid core. Only for high *Da*, one can observe comparable fluid motion in both the porous medium and central fluid core regions. The local Nusselt number on the surface and interface temperature exhibit nearly uniform variations for low *Da*. For high *Da*, marked heat transfer is observed on the bottom of the sphere. The interface temperature is also seen to deviate from uniform variation for high *Da*.

(4) The intensity of the recirculating flow in the central fluid core region was seen to depend on the thermal conductivity ratio. The thermal conductivity ratio modifies the time scale of the thermal transport and only the relative magnitudes of the monitored quantities are affected.

References

[1] S.P. Pustovoit, Transient thermal convection in a spherical cavity, P.M.M. (Journal of Applied Mathematics and Mechanics) 22 (1958) 568–572.

[2] H.G. Whitley III, R.I. Vachon, Transient laminar free convection in closed spherical containers, Transactions of the ASME, Journal of Heat Transfer 94 (1972) 360–366.

[3] M.Y. Chow, R.G. Akins, Pseudosteady-state natural convection inside spheres, Transactions of the ASME, Journal of Heat Transfer 97 (1975) 54–59.

[4] J. Hutchins, E. Marschall, Pseudosteady-state natural convection heat transfer inside spheres, International Journal of Heat and Mass Transfer 32 (1989) 2047–2053.

[5] F. Shen, J.M. Khodadadi, Y. Zhang, Pseudosteady-state natural convection inside spherical containers, in: Proceedings of the Fourth ASME/JSME Thermal Engineering Joint Conference, vol. 1, ASME, NY, 1995, pp. 209–216.

[6] H.D. Nguyen, S. Paik, I. Pop, Transient thermal convection in a spherical enclosure containing a fluid core and a porous shell, International Journal of Heat and Mass Transfer 40 (1997) 379–392.

[7] K. Vafai, C.L. Tien, Boundary and inertia effects on flow and heat transfer in porous media, International Journal of Heat and Mass Transfer 24 (1981) 195–203.

[8] G. de Vahl Davis, A note on a mesh for use with polar coordinates, Numerical Heat Transfer 2 (1979) 261–266.

[9] S.V. Patankar, Numerical Heat Transfer and Fluid Flow, Hemisphere Publishing Corporation, Washington, DC, 1980.